A numerical study of the influence of microvoids in the transverse mechanical response of unidirectional composites

Danial Ashouri Vajari , Carlos González , Javier Llorca , Brian Nyvang Legarth

A B S T R A C T

The effect of porosity on the transverse mechanical properties of unidirectional fiber-reinforced composites is studied by means of computational micromechanics. The composite behavior is simulated by the finite element analysis of a representative volume element of the composite microstructure in which the random distribution of fibers and the voids are explicitly included. Two types of voids – interfiber voids and matrix voids – were included in the microstructure and the actual damage mechanisms in the composite, namely matrix and interface failure, were accounted for. It was found that porosity (in the range 1–5%) led to a large reduction in the transverse strength and the influence of both types of voids in the onset and propagation of damage throughout the microstructure was studied under transverse tension and compression. Finally, the failure locus of the composite lamina under transverse tension/compression and out-of-plane shear was obtained by means of computational micromechanics and compared with the predictions of Puck's model and with experimental data available in the literature. The results show that the strength of composites is significantly reduced by the presence of voids.

1. Introduction

The combination of stiff glass-fibers embedded in low density polymers leads to a lightweight material with outstanding stiffness, strength and creep resistance. However, composite materials present different physical failure mechanisms as a function of loading conditions. At the microscopic level, failure is controlled by the brittle nature of epoxy matrix, the decohesion of the fiber/matrix interface and the presence of defects (voids, delaminations).

Numerical simulation is becoming a powerful tool to understand the failure processes and subsequently design of composite materials. Within the realm of the micromechanical simulation of the deformation and failure processes, two different strategies have been developed. The first one assumes that the fibers are regularly distributed within the ply, which leads to a simplified unit-cell model including few fibers (normally one or two). For instance, París et al. [1] studied interface debonding by modeling a single-fiber unit cell embedded in polymer matrix. In a similar model, Correa et al. [2] studied the initiation and propagation of an interface crack which subsequently kinks into the matrix. Romanowicz [3] computationally predicted the failure locus of a two-fiber unit-cell using a bi-linear cohesive zone at the fiber/matrix interface and the Drucker–Prager criterion to consider the pressure-dependent yielding of polymers. Although these unit-cell studies provided valuable insights into the micromechanisms of deformation and fracture, their results cannot be extrapolated to predict the behavior of actual composite plies because the regular fiber distribution is not realistic.

The second modeling approach considers an RVE including several dozens of fibers which are randomly distributed in the matrix. The size of the microstructure included in the RVE is large enough so that the effective properties are independent of the RVE size and of the position of fibers. Gonzàlez and Llorca [4] and Totry et al. [5] validated the multi-fiber RVE modeling strategy with experiments to determine the fracture behavior of composite under different loading modes. The matrix in these studies was assumed to follow the Coulomb–Mohr yield criterion. Interface debonding was modeled by a bi-linear cohesive zone model.

Special attention must be given to the role of defects and, in particular, of voids due to their influence on the mechanical performance of composite materials. Voids can be found in different shapes and sizes and there are two principal sources. The first one is air entrapment in the composite (particularly between plies)

during lay-up. In addition, voids may be formed by volatile components or contaminants which vaporize during the high-temperature part of the composite cure cycle [6]. Typical voids found in glass-fiber polymer composites used in wind turbines are found in Fig. 1. Fig. 1a shows large voids as compared to the fiber diameter, while Fig. 1b provides a closer view of microvoids whose size is comparable or smaller than the fiber diameter. These microvoids appear normally between the fibers where the matrix cannot easily flow in during manufacturing or they can also be originated due to very small air bubbles being trapped in the matrix. It is well established that porosity reduces the mechanical properties of fiber-reinforced composites controlled by the matrix (interlaminar shear strength, transverse strength as well as modulus, fatigue resistance, etc., see Thomason [6]). Experimental work has been also carried out to assess the effect of voids on the mechanical behavior of composites. Hernández et al. [7] studied the effect of temperature cycle on the void volume fraction, shape and spatial distribution in composites using X-ray microtomography. Regardless of the final porosity, voids were elongated and oriented parallel to the fibers. Detailed studies of the effect of porosity on the transverse mechanical properties of UD laminates are limited. Olivier et al. [8] analyzed the effect of porosity on the transverse tensile strength while several investigations [8–11] studied the influence of void volume fraction on the interlaminar shear strength. Porosity always reduced significantly the shear strength but there were large differences among different materials. This was attributed to the influence of void size, shape and spatial distribution.

Several numerical studies have also been conducted to evaluate the effect of voids in epoxies. Chew et al. [12] and Cheng and Guo [13] studied the void interaction and coalescence in polymers. They showed that microvoid cavitation, enhanced by strain softening, accelerates the process of void coalescence resulting in brittle-like failure at lowered stresses and strains. Moraleda et al. [14] studied the finite deformation of porous elastomers by selecting an RVE containing a random distribution of circular voids. Nevertheless, to the authors' knowledge, the effect of microvoids on the mechanical response of composites has not been simulated within the framework of multi-void/fiber RVEs in which both are randomly distributed in the matrix and this is the main objective of this investigation. The geometrical model provides a realistic representation of the composite microstructure, which explicitly considers the spatial distribution of fibers, matrix, interfaces and voids. This work focuses on the microvoids shown in Fig. 1b whose diameters are small and are found between fibers. The effect of volume fraction, size and position of voids on the overall stress–strain response of UD composites will be analyzed. As a result of these analyses, the failure locus including the effect of porosity will be obtained for UD composites subjected to transverse tension/compression and out-of-plane shear.

2. Problem formulation

Microvoids may be arbitrarily shaped, which requires an expensive full 3D simulation. However, experiments by Little et al. [15] and Hernández et al. [7] have shown that micron-sized voids within composite plies were elongated and oriented along the fiber direction. They found that the void aspect ratio (length/average diameter) was in the range 10–40 and the void aspect ratio increased with the void volume. They have also shown that $\sim 45\%$ of the voids have a diameter less than 50 μm and $\sim 20\%$ of the voids have a diameter below 20 μm [15]. These observations indicate the presence of cylindrical microvoids, which can be modeled in 2D in a similar way as the fibers.

A schematic of the microstructure of UD composites including fibers, matrix and microvoids is depicted in Fig. 2a. The corresponding square cell is shown in Fig. 2b, which includes the distribution of dozens of circular fibers, circular microvoids and microvoids isolated between the fibers. Obviously, this 2D representation considers that all voids and fibers are cylindrical. A Cartesian reference coordinate system, x_i, is placed at the bottom-left corner of the cell and aligned with its edges (Fig. 2b). The positive direction of the first axis, x_1, points in the out-of-plane normal direction to the (x_2, x_3)-plane. The dimension of the cell is determined by the length, L, the width, W, the radius of the N_f monosized fibers, R_f, which yields the fiber volume fraction $V_f = N_f \pi R_f^2 / WL$. The total void volume fraction, V_v, is the sum of the void volume fraction of the N_v circular voids of radius R_v^i, $\sum_{i=1}^{N_v} \pi {R_v^i}^2 / WL$, plus the void volume fraction due to the trapped voids isolated between the fibers (four shown in Fig. 2b). The cell in these analyses is always a square cell with $L = W = L_0$. The cell is subjected to incremental normal tension or compression in the transverse direction by imposing $\dot{\Delta}_3$ as well as to out-of-plane incremental shear specified by $\dot{\Delta}_{23}$, as shown in Fig. 2b.

The cell contains a random distribution of 70 monosized fibers of radius $R_f = 0.1 L_0$ leading to the fiber volume fraction of $\sim 60\%$ and void volume fraction of 1—5%, which are realistic values for composites of good quality. The nearest fiber distance is set to a minimum value to avoid fiber overlap during the generation of the RVE. The majority of this porosity is in voids trapped between fibers and the rest are isolated voids dispersed in the matrix. Fibers and voids intersecting the cell edges were split and copied to the opposite sides of the square cell to create a periodic microstructure. Periodic boundary conditions were applied to the edges of the cell to ensure the continuity between neighboring cells (which may deform like jigsaw puzzles). The periodic boundary conditions can be expressed in terms of the prescribed displacement vectors $\vec{U}_2$ and $\vec{U}_3$ which relate the displacements, $\vec{u}$, between opposite edges according to

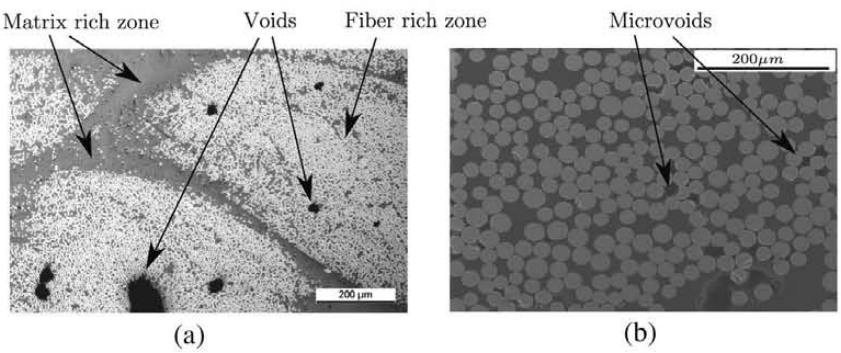

Fig. 1. Shape and size of voids in composites used in wind turbine blades. (a) Large voids, as compared to the fiber diameter. (b) Position and shape of microvoids whose size is comparable or smaller than the fiber diameter.

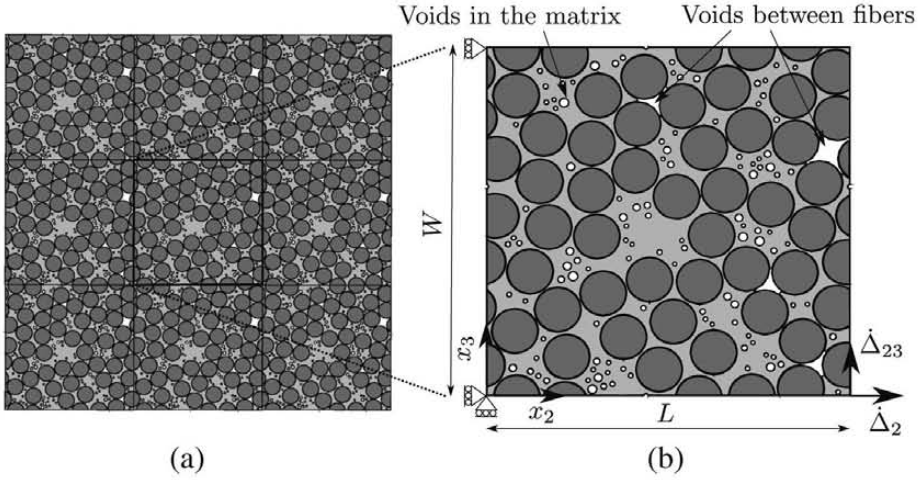

Fig. 2. (a) Illustration of the fiber and void distribution in a cross-section of a fiber-reinforced composite. (b) Unit cell of the porous fiber-reinforced composites. The dimensions, loads and the coordinate system are shown. The cell can be subjected to transverse tension/compression by applying $\dot{\Delta}_2$ and out-of-plane shear by applying $\dot{\Delta}_{23}$.

$$\begin{aligned}\vec{u}(0,x_3)-\vec{u}(L_0,x_3)&=\vec{U}_2\\ \vec{u}(x_2,0)-\vec{u}(x_2,L_0)&=\vec{U}_3\end{aligned} \tag{1}$$

Combined uniaxial tension/compression along the x_2-axis and out-of-plane shear are imposed with $\vec{U}_2=(\Delta_2,\Delta_{23})$ and $\vec{U}_3=(u_2,u_3)$, where Δ_2 denotes the compression or tension load depending on the sign of Δ_2 and Δ_{23} defined the shear deformation. While the component of u_2 is determined from the condition of mechanical equilibrium, u_3 is computed so that the average normal stresses perpendicular to the tension/compression axis (x_2) is zero. The incremental tensile/compressive and shear strains are given by

$$\dot{\epsilon}_2=\frac{\dot{\Delta}_2}{L_0}\quad\text{and}\quad\dot{\gamma}_{23}=\arctan\left(\frac{\dot{\Delta}_{23}}{L_0}\right) \tag{2}$$

The corresponding normal and shear stresses are computed from the resultant normal and tangential forces acting on the edges divided by the actual cross-section, A, as

$$\sigma_2=\frac{1}{A}\int T_2 t dx_3\Big|_{x_2=L_0}\quad\text{and}\quad\tau_{23}=\frac{1}{A}\int T_3 t dx_3\Big|_{x_2=L_0} \tag{3}$$

where t is the unit thickness of the cell in the x_1-direction and T_2 and T_3 denote the normal and shear traction at the edge $x_2=L_0$, respectively.

3. Material model

3.1. Isotropic modified Drucker–Prager model

The matrix behavior corresponds to an isotropic epoxy resin and fails at a very low strain in a brittle fashion under uniaxial tension [16]. Under uniaxial compression or shear, epoxy resins undergo considerable plastic deformation and the flow stress is pressure-dependent [16–18]. The Drucker–Prager yield criterion has often been used to model the mechanical behavior of these materials. As illustrated in Fig. 3, this model is a modification of the von Mises criterion with different tensile and compressive yield stress (shown as a dashed-line in Fig. 3). In addition, the Drucker–Prager yield criterion includes the effect of hydrostatic stresses on the flow stress by including an additional term in the von Mises expression, according to

$$F(I_1,J_2)=\sqrt{3J_2}+\alpha I_1-c=0 \tag{4}$$

where I_1 is the first invariant of the stress tensor, J_2 is the second invariant of the deviatoric stress tensor and c is the flow stress under pure shear. The pressure-sensitivity parameter, α, can be determined by Lubliner et al. [19]

$$\alpha=\frac{\frac{\sigma_m^{b0}}{\sigma_m^{c0}}-1}{2\frac{\sigma_m^{c0}}{\sigma_m^{t0}}-1} \tag{5}$$

Here, σ_m^{c0}, σ_m^{b0} and σ_m^{t0} denote the matrix uniaxial compressive yield stress, the biaxial compressive yield stress and the uniaxial tensile yield stress, respectively, see Fig. 3. In order to include the brittle behavior of the epoxy matrix in tension, the modified Drucker–Prager model developed by Lubliner et al. [19] and Lee and Fenves [20] was used in this investigation to simulate the matrix behavior. It is expressed by

$$F(I_1,J_2,\sigma_l,\beta,\alpha)=\frac{1}{1-\alpha}\left(\sqrt{3J_2}+\alpha I_1+\beta\langle\sigma_l\rangle\right)-\sigma_m^{c0}=0 \tag{6}$$

where σ_l is the maximum principal stress, $\langle\rangle$ denotes the Macaulay brackets (which return the argument if positive and zero otherwise), and β is a function of the tensile, σ_m^{t0}, and compressive, σ_m^{c0}, yield stress according to

$$\beta=\frac{\sigma_m^{c0}}{\sigma_m^{t0}}(1-\alpha)-(1+\alpha) \tag{7}$$

The yield surface corresponding to the modified Drucker–Prager criterion is depicted in Fig. 3. It follows the standard Drucker–Prager yield criterion with an associated flow rule under compression, which has been experimentally validated for glassy polymers [17]. Chew et al. [12] and Quinson et al. [17] discussed that the pressure-sensitivity reduces the load-carrying capacity and influences the strain for void coalescence, and also showed that plastic dilatancy effects are relatively milder. Thus, for the sake of simplicity, an associated flow rule is considered to simulate the plastic flow of the matrix. The epoxy behavior in tension was controlled by the maximum principal stress and the yield surface was cut off by the tensile yield stress, σ_m^{t0}, as shown with the straight dashed lines in Fig. 3.

The stress–strain behavior of the matrix under uniaxial compression and uniaxial tension is shown in Fig. 4. Plastic deformation at constant flow stress occurred in compression after yielding, leading to failure by the localization of a shear band. In Fig. 4, σ_m^{cu} denotes the matrix ultimate compressive strength. Conversely, the behavior in tension was brittle due to microcracking and this is accounted for by a softening law [21]. The energy dissipated by a unit volume during tensile cracking is G_m which is the area under the tensile stress–strain curve for $\epsilon_m>0$. Residual

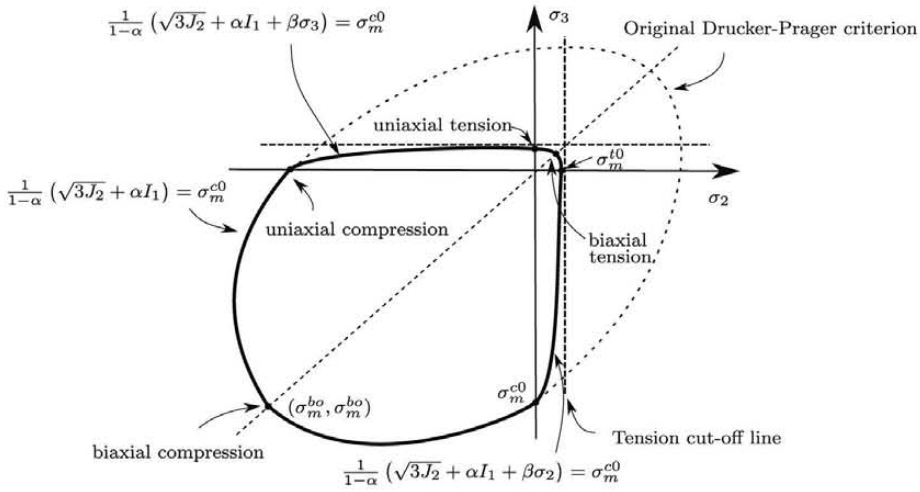

Fig. 3. Yield surface of the modified Drucker–Prager criterion. The dashed-line denotes the original Drucker–Prager criterion.

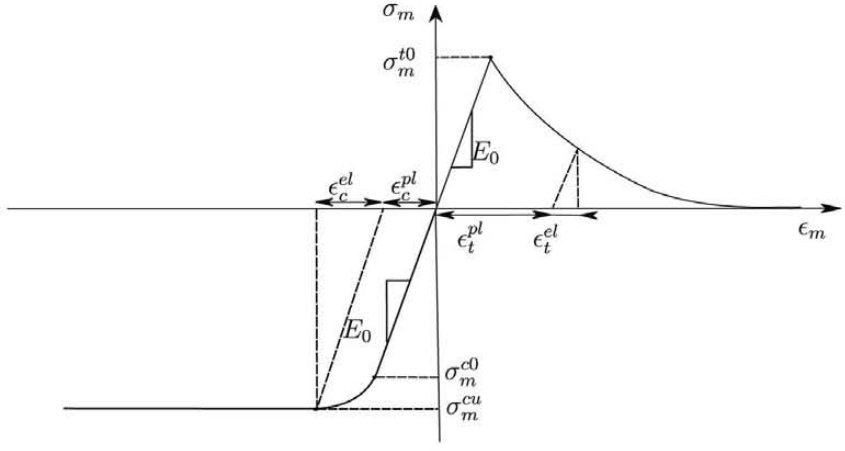

Fig. 4. Stress–strain behavior of the matrix under uniaxial tension and uniaxial compression.

stresses due to chemical cure shrinkage and cooling from processing temperature were not taken into account, as this investigation was focussed in the effect of porosity.

Glass-fibers were modeled as isotropic, elastic materials whereas the matrix properties correspond to typical values used in the modified Drucker–Prager model for an epoxy matrix [21]. The pressure-sensitivity parameter was chosen to be $\alpha = 0.13$ which is within the range reported by Quinson et al. [17] and Chew et al. [12].

3.2. Cohesive zone model

The fiber/matrix interface was modeled using a cohesive zone model, which relates the normal and tangential stresses transferred through the crack with the normal and tangential crack opening [22]. In this model, λ is defined as a non-dimensional parameter describing the separation between the crack faces as

$$\lambda = \sqrt{\left(\frac{u_n}{\delta_n^c}\right)^2 + \left(\frac{u_t}{\delta_t^c}\right)^2} \tag{8}$$

such that damage initiation starts at a specified value, $\lambda = \lambda_2$, and fully damage occurs when $\lambda \geqslant 1$. δ_n^c and δ_t^c stand for the normal and tangential characteristic cohesive lengths, respectively, and u_n and u_t are the normal and tangential separation between the crack faces, respectively. As shown in Fig. 5, $\sigma(\lambda)$ defines a traction potential as

$$G_{int} = \delta_n^c \int_0^{\lambda} \sigma(\lambda) d\lambda \tag{9}$$

where the area under $\sigma(\lambda)$ represents the fracture energy, G_{int}. Therefore, the normal, T_n, and tangential, T_t, tractions acting on the interfaces are defined from Eq. (9) as

$$T_n = \frac{\partial G_{int}}{\partial u_n} = \frac{\sigma(\lambda)}{\lambda}\frac{u_n}{\delta_n^c}, \qquad T_t = \frac{\partial G_{int}}{\partial u_t} = \frac{\sigma(\lambda)}{\lambda}\frac{\delta_n^c}{\delta_t^c}\frac{u_t}{\delta_t^c} \tag{10}$$

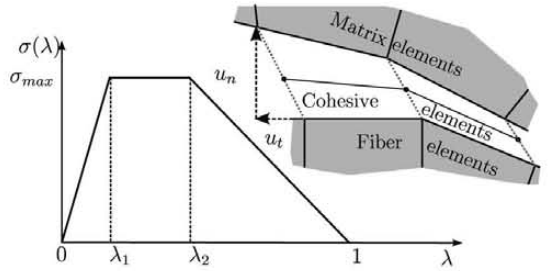

Fig. 5. Traction–separation law used to characterize interface separation.

The incremental traction vector is related to the displacement increments across the interface as

$$\begin{bmatrix} \dot{T}_t \\ \dot{T}_n \end{bmatrix} = \begin{bmatrix} \frac{\partial T_t}{\partial u_t} & \frac{\partial T_t}{\partial u_n} \\ \frac{\partial T_n}{\partial u_t} & \frac{\partial T_n}{\partial u_n} \end{bmatrix} \begin{bmatrix} \dot{u}_t \\ \dot{u}_n \end{bmatrix} \tag{11}$$

where the matrix on the right hand side is the cohesive tangent modulus.

The interface behavior is controlled by the cohesive strength, σ_{max}, and the interface fracture energy, G_{int}. The cohesive strength was chosen to be equal to 50 MPa, following the experimental results obtained by Canal et al. [21]. The interface fracture energy was $G_{int} = 10\,\mathrm{J/m^2}$, one tenth of the matrix fracture energy, $G_m = 100\,\mathrm{J/m^2}$. As the interface fracture energy is given by the area under the cohesive traction–separation law, it follows

$$G_{int} = \frac{\sigma_{max}(1 + \lambda_2 - \lambda_1)\delta_n^c}{2} \tag{12}$$

where $\lambda_1 = 10^{-3}$ and $\lambda_2 = 10^{-1}$. Substituting σ_{max}, G_{int}, λ_1 and λ_2 into Eq. (12) yields $\delta_n^c = \delta_t^c \simeq 0.4\,\mu\mathrm{m}$.

4. Numerical methods

Simulations are carried out with Abaqus/Standard [23] under plane strain conditions within the framework of the finite deformations theory with the initial unstressed state as reference. The matrix and the fibers were automatically meshed using 3-node isoparametric triangles. An example of finite element mesh is shown in Fig. 6. In addition, 4-node interface elements were inserted at the fiber/matrix interface to include the effect of interface decohesion. The converged finite element discretization includes around 48,000 solid elements, 3350 cohesive elements and 56,000 nodes. Totry et al. [5] discussed that different arrangement of fibers in an RVE including 30 fibers with interface debonding under uniaxial compression shows up to 7% deviation in the ultimate failure stress. This scatter can be even larger when the RVE includes voids. This work does not aim at studying an RVE which macroscopically represents the lamina but focuses on the effect of voids randomly distributed in the matrix.

5. Results and discussion

5.1. Influence of porosity on the failure mechanisms

The matrix properties, as a typical thermosetting epoxy, are $E_m = 3$ GPa, $\nu_m = 0.3$, $\sigma_m^{c0} = 85$ MPa, $\sigma_m^{cu} = 95$ MPa, $\sigma_m^{t0} = 65$ MPa, $\alpha = 0.13$ and $G_m = 100\,\mathrm{J/m^2}$ and the material properties of the glass fibers are $E_f = 70$ GPa and $\nu_f = 0.21$. While the cohesive parameters are assumed to be $\delta_n^c = \delta_t^c = 0.4\,\mu$m, $\sigma_{max} = 50$ MPa and $G_{int} = 10\,\mathrm{J/m^2}$. These material parameters are unchanged throughout the paper.

Fig. 7a shows the macroscopic stress–strain under transverse tension for an RVE containing a fiber volume fraction $V_f = 60\%$ and void volume fraction $V_v = 2\%$. The initial elastic response is followed by a non-linear hardening region up to a maximum (point A in Fig. 7a). Afterwards, the load bearing capacity is rapidly reduced as a result of unstable crack growth in the fiber/matrix interfaces along the RVE. The damage sequence within the RVE is shown in Fig. 7d for the points A, B, and C, respectively, in the stress–strain curve. These plots show that the first damage mechanism, responsible for the non-linearity above 25 MPa and for the maximum strength, was interface decohesion. Interface cracks initiated around voids trapped between fibers (Fig. 7b). The composite strength was $\approx$ 37 MPa, below the matrix strength in tension (σ_m^{t0} = 65 MPa) and the interface strength (σ_{max} = 50 MPa), and this was due to the presence of the voids, that triggered the onset of interface decohesion at lower stresses. Damage propagated by the successive fracture of interfaces (Fig. 7c) and the crack path was also influenced by the location of interfiber voids. Load was carried by the matrix ligaments between decohered interfaces in the last stages of deformation (Fig. 7d), and final fracture occurred by the link up of interface cracks through the epoxy resin. This series of events is in excellent agreement with recent *in situ* fracture tests under transverse tension carried out within a scanning electron microscope, which showed the same sequence of damage [21].

The influence of the size of the circular voids within the matrix on the stress–strain response under transverse tension is plotted in Fig. 8a, which includes the curves corresponding to the composite without voids and the composite with a void volume fraction V_v = 1.5%. The fiber volume fraction (60%) and the fiber spatial distribution was identical in all cases. As in the previous case, two types of voids were placed in the composite: voids trapped

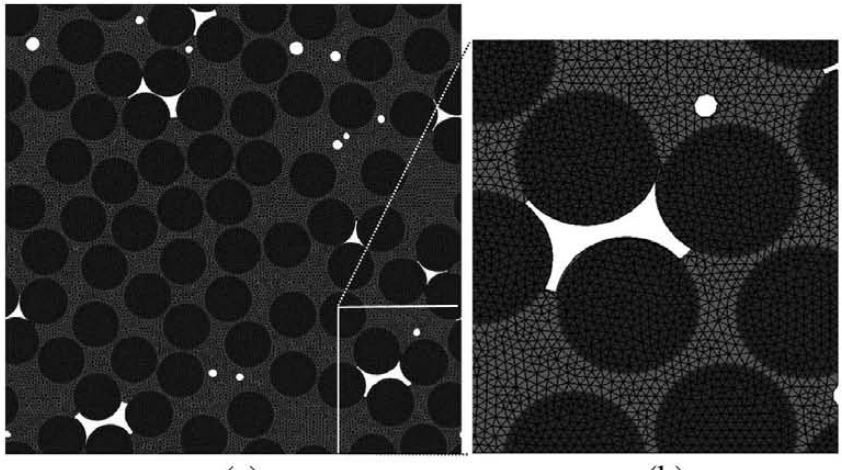

Fig. 6. Finite element mesh of the cell. The mesh includes around 48,000 solid elements, 3350 cohesive elements and 56,000 nodes. The red line between the fibers and the matrix denotes the cohesive elements. (For interpretation of the references to colour in this figure legend, the reader is referred to the web version of this article.)

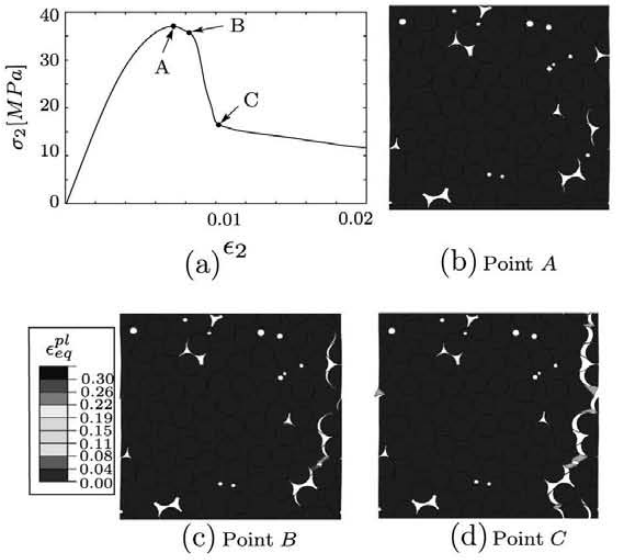

Fig. 7. (a) Stress–strain response under transverse tension of an RVE containing $V_f = 60\%$ and $V_v = 2\%$. Contour plot of the equivalent plastic strain within the RVE for: (b) Point A in the stress–strain curve. (c) Point B in the stress–strain curve. (d) Point C in the stress–strain curve. The displacements are magnified by a factor of 3 in the contour plots.

between fibers and circular isolated voids dispersed in the matrix. While the size and distribution of the interfiber voids were the same in all RVEs, different values of the average radius of the circular voids, $\bar{R}_v = 0.2R_f$, $0.3R_f$ and $0.4R_f$, were chosen for each RVE. The void-free material presented the highest strength, which was close to the interface strength (50 MPa), indicating that interface fracture controlled the maximum bearing capacity of the composite under transverse tension. The analysis of the failure micromechanisms close to the peak load ($\epsilon_2 = 0.9\%$) showed that interface decohesion perpendicular to the tensile stress was the dominant fracture mode Fig. 8b.

The presence of 1.5% porosity reduced the composite strength by ≈20% but the size of the circular voids within the matrix did not influence the transverse tensile strength (Fig. 8a). There were, however, significant changes in the post-peak behavior because the damage localization path changed with the void size, as shown in the contour plots of the equivalent plastic strain depicted in Fig. 8e. While the initial damage (and, thus, the strength) was always controlled by the interfiber voids, the final crack path depended on the circular void size. Large voids can change the path of cracks (Fig. 8e) while the crack path was insensitive to the presence of small voids (Fig. 8c). This effect of the void size (or void distribution) on the post-peak behavior is equivalent to the influence of the fiber spatial distribution because the final damage localization path is very sensitive to the microstructural details (fiber and void spatial distribution and size) of the RVE.

The effect of porosity and of the void size on the mechanical response under transverse compression is shown in Fig. 9a. The RVE corresponding to the four stress–strain curves are identical to those used to compute the mechanical behavior under transverse tension in Fig. 8. The numerical simulations showed that the presence of 1.5% of voids reduced the compressive strength only by ≈14%, as compared with a reduction of ≈20% under transverse tension. These differences can be attributed to the change in the failure mechanisms which control fracture upon tension or compression. Failure under transverse compression takes place by the localization of the plastic strain in the matrix, which leads to the formation of a shear band (Fig. 9b). The angle between the shear band and the direction perpendicular to the loading axis was slightly higher than 45° (in the range of 50–56°) and this was attributed to the pressure sensitivity of matrix yield strength [4]. The contour plots of the void-free and porous RVEs after the peak load are depicted in Fig. 9b–e and demonstrate that the presence of voids did not change the dominant failure mechanism. In addition, the orientation of the shear band was around 55°, within the expected range for fully-dense composites. More detailed analysis of these plots show that the localization band started at interfiber voids, which acted as stress concentrators, and were again responsible for the reduction in strength. The final localization path was controlled by the pressure sensitivity of the matrix and also by the presence of the circular voids in the matrix, which attracted the shear band. This effect of the circular voids seemed

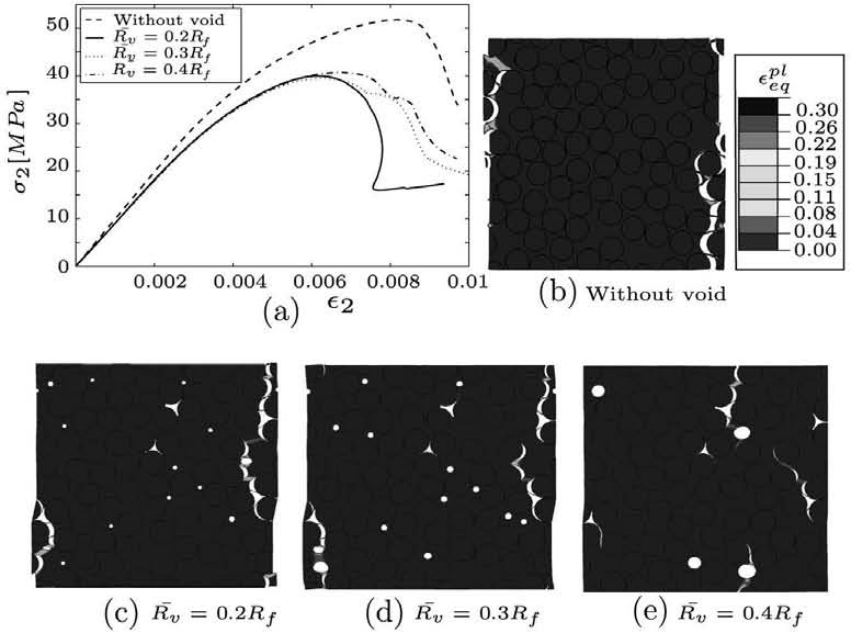

Fig. 8. Effect of void size on the mechanical behavior under transverse tension of an RVE containing $V_f = 60\%$ and $V_v = 1.5\%$. (a) Stress–strain response. Contours plots of the equivalent plastic strain at $\epsilon_2 = 0.009$ in the RVE for: (b) Void-free material. (c) Porous material with an average radius of the circular voids $\overline{R_v} = 0.2R_f$, (d) $\overline{R_v} = 0.3R_f$ and (e) $\overline{R_v} = 0.4R_f$. The displacements are magnified by a factor of 3 in the contour plots.

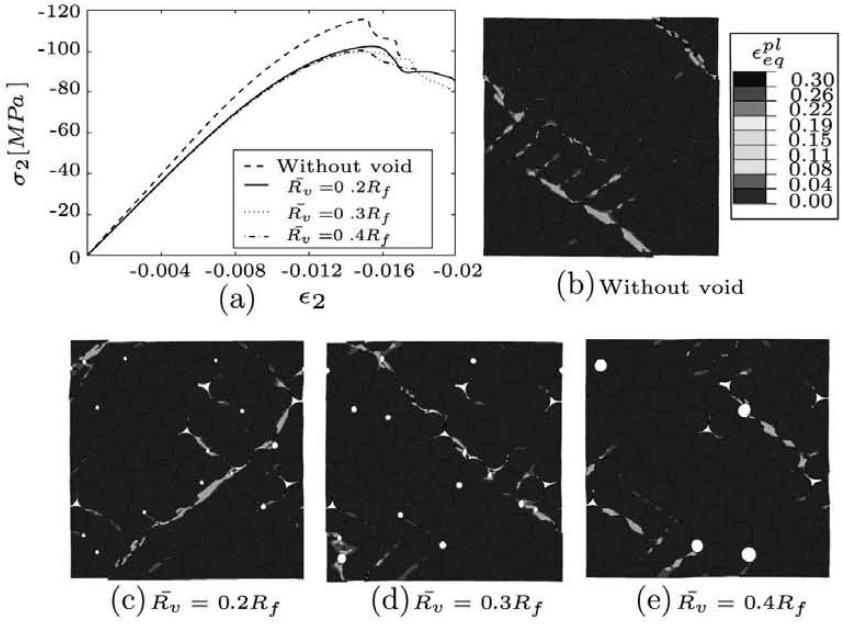

Fig. 9. Effect of void size on the mechanical behavior under transverse compression of an RVE containing $V_f = 60\%$ and $V_v = 1.5\%$. (a) Stress–strain response. Contours plots of the equivalent plastic strain at $\epsilon_2 = -0.016$ in the RVE for: (b) Void-free material. (c) Porous material with an average radius of the circular voids $\overline{R_v} = 0.2R_f$, (d) $\overline{R_v} = 0.3R_f$ and (e) $\overline{R_v} = 0.4R_f$. The displacements are magnified by a factor of 3 in the contour plots.

to increase with the void size, as it happened under transverse tension.

The overall effect of the void volume fraction in the mechanical behavior under transverse tension and compression can be found in the stress–strain curves plotted in Fig. 10a and b, respectively. The curves in these plots were obtained in an RVE containing a fiber volume fraction of 60% and porosity levels in the range 0–5%. The proportion of interfiber voids was 0.7%, 1.5% and 2.5% in the RVEs with V_v = 1%, 2% and 5%, respectively and the remaining were the circular voids embedded in the matrix. This porosity range was selected because composite materials for aerospace require porosity levels below 1–2% while porosity of up to 5% can be tolerated in other applications [24]. In both cases (tension and compression), porosity reduced the composite strength. No experimental results on the effect of porosity on the transverse compressive strength were found in the literature. Olivier et al. [8] has detailed information about the influence of porosity on the transverse tensile strength of UD composites. The experimental data in that paper reported that the transverse tensile strength was reduced by approximately 7% and 20% in the presence of 5% of porosity in two different carbon-fiber/epoxy composites with 60% fiber volume fraction. The numerical predictions in Fig. 10a for 5% porosity were slightly higher (around 30%). Moreover, the numerical study highlighted different influences of voids under transverse tension and compression. On the former events, small amounts of porosity (1%) reduced markedly the transverse tensile strength and increasing the void volume fraction up to 5% did not have very negative effects on the strength. This behavior was a result of the dominant failure mechanism, brittle interface decohesion. Interfiber voids were very efficient to promote interface decohesion at low stresses and the stress concentration at the crack tip propagated damage rapidly through the microstructure. Only one or two voids are necessary to trigger this process and increasing the void volume fraction did not reduce much further the tensile strength. The formation of a shear band through the matrix is, however, a ductile process and the maximum bearing capacity of the composite is not only controlled by the initiation of the shear band but by the propagation throughout the microstructure. This latter process is easier in the presence of larger porosity and thus the transverse compressive strength decreased rapidly with the void volume fraction.

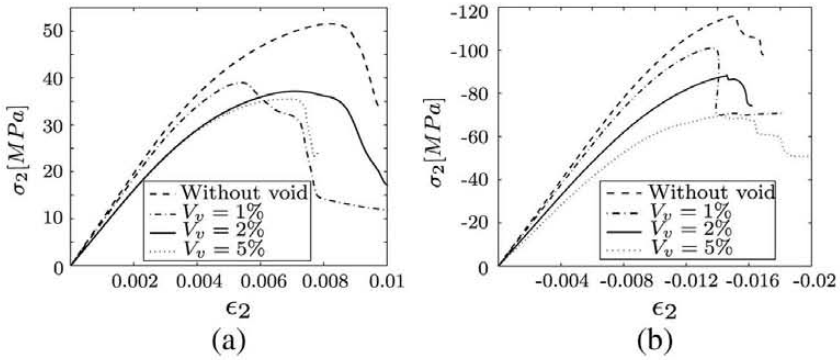

Fig. 10. Effect of void volume fraction on the mechanical behavior of UD fiber-reinforced composites. (a) Transverse tension. (b) Transverse compression.

5.2. Influence of porosity on the failure envelope

Laminate design is based on failure criteria in the stress space which are formed by the intersection of various smooth surfaces, each one representing the critical condition for a given fracture mode. There are different classical failure criteria such as Tsai–Hill, Tsai–Wu, the recently developed NU theory [25] and Puck's criterion all to be used in composite design. Puck's criterion has been largely consistent with the experimental results of the failure envelope of a composite made up of a brittle epoxy matrix reinforced with either glass or C fibers [26] as well as with the numerical results obtained for these composites using computational micromechanics [5]. Puck's criterion is based on the Hashin's failure criterion [27], who distinguished between fiber- and matrix-dominated fracture, and each one was further subdivided into tensile and compressive modes. Furthermore, he assumed that failure was due to the normal and tangential stresses acting on the fracture plane, which is parallel to the fibers in the case of matrix-dominated failure in tension. Puck and Schürmann [18] improved Hashin's model by assuming that failure was caused by the normal, σ_n, and tangential, τ_t, stresses acting on the failure plane, which forms a fracture angle, θ_f, with the direction perpendicular to the tensile stresses. The fracture angle was explicitly determined for each combination of normal, σ_2, and shear, τ_{23}, stresses acting on the lamina. The fracture angle under compression is predicted to be 50°. Puck's failure criterion is then expressed as

$$\sqrt{\left[\left(\frac{1}{Y_T}-\frac{2p_{\perp\perp}(1+p_{\perp\perp})}{Y_C}\right)\sigma_n(\theta_f)\right]^2+\left[\frac{2(1+p_{\perp\perp})}{Y_C}\tau_t(\theta_f)\right]^2}+\frac{2p_{\perp\perp}(1+p_{\perp\perp})}{Y_C}\sigma_n(\theta_f)=1 \quad \text{for} \quad \sigma_n \geqslant 0 \tag{13}$$

$$\sqrt{\left[\frac{2(1+p_{\perp\perp})}{Y_C}\tau_t(\theta_f)\right]^2+\left[\frac{2p_{\perp\perp}(1+p_{\perp\perp})}{Y_C}\sigma_n(\theta_f)\right]^2}+\frac{2p_{\perp\perp}(1+p_{\perp\perp})}{Y_C}\sigma_n(\theta_f)=1 \quad \text{for} \quad \sigma_n < 0 \tag{14}$$

with

$$\begin{aligned}\sigma_n(\theta_f) &= \sigma_2\cos^2\theta_f + 2\tau_{23}\sin\theta_f\cos\theta_f\\ \tau_t(\theta_f) &= -\sigma_2\sin\theta_f\cos\theta_f + \tau_{23}\left(\cos^2\theta_f-\sin^2\theta_f\right)\end{aligned} \tag{15}$$

where Y_T and Y_C stand for the transverse tensile and compressive strength of composite, respectively. θ_f denotes the fracture plane orientation under transverse compression, which is always 0° under transverse tension. The inclination coefficient, $p_{\perp\perp}$, is a fitting parameter in the range of 0.20—0.25 for glass-fiber/epoxy composites [18]. Puck's model is controlled by the tensile and the compressive transverse strength. This information for composite with different void volume fraction can be obtained from the numerical simulation, as shown in the previous section.

The failure locus in σ_2–τ_{23} stress space is plotted in Fig. 11 for a composite lamina containing 60% of glass fibers and different porosities (no voids and V_v = 1%, 2% and 5% of which the proportion of interfiber voids was 0.7%, 1.5% and 2.5%, respectively and the remaining were circular voids embedded in the matrix). The predictions of Puck's model with $p_{\perp\perp} = 0.22$ can be compared in Fig. 11 with solid points provided by computational micromechanics. They were obtained by the numerical simulation of an RVE subjected to a different loading paths characterized by different ratios of the normal to the shear displacement, Δ_2/Δ_{23} while $\sigma_3 = 0$. The strength under biaxial loading (transverse tension or compression and out-of-plane shear) was determined by the point at which one (or often both) normal and shear stresses began to decrease as the normal and shear displacements increase.

In addition to Fig. 10 which indicated the effect of porosity in reduction of transverse tension and compression, Fig. 11 also shows the large influence of porosity on the transverse shear strength of UD fiber-reinforced composites. Several authors reported experimental results on the influence of porosity on the shear strength of UD fiber-reinforced composites [8–11]. The composites were reinforced with either glass or carbon fibers and with similar fiber volume fraction to our RVE. The experimental reduction in the shear strength for a porosity of 5% was in the range 15–40%, which is in good agreement with the numerical predictions in Fig. 11 which shows 35% reduction for V_v = 5%. Again, the experimental scatter seems to be controlled by the size, shape and spatial distribution of voids and the present numerical strategy seems to be a promising tool to capture the effect of these factors.

The predictions of the Puck's model (based on the computationally provided values of the strength under transverse tension and compression) were in very good agreement with the results provided by computational micromechanics. This comparison supports the validity of the computational model to predict different physical failure mechanisms occurring in UD laminates and the shape of the failure envelope for the combined transverse normal and shear loading conditions. This agreement indicates that the dominant damage mechanisms are not modified although porosity reduced the strength of composites by triggering damage at lower stresses. However, it should be noted that the available failure criteria (such as Puck's model) cannot explicitly predict the strength reduction due to porosity as they need experimental data (strength in tension and compression of the porous composite) as input. On the contrary, micromechanics simulations are able to determine

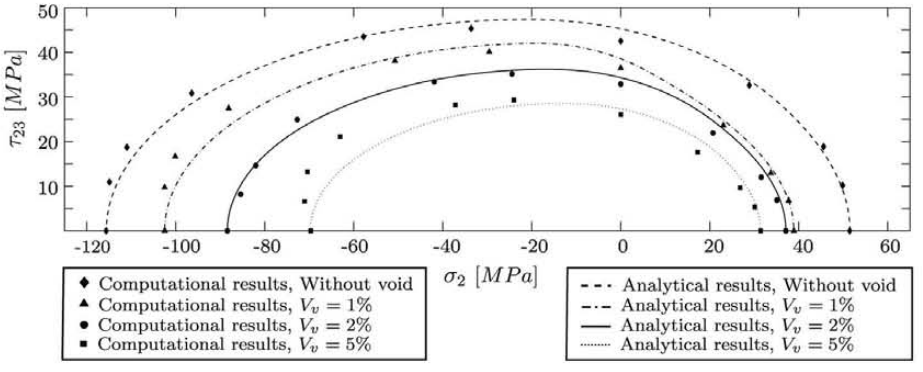

Fig. 11. Failure locus of a UD fiber-reinforced composite in the σ_2—τ_{23} stress space as function of porosity. The lines correspond to the predictions of the Puck's model [18]. The solid symbols stand for the numerical predictions obtained from the numerical simulation of an RVE of the microstructure.

the failure locus based on the microstructural features (e.g., the fiber, matrix and interface properties, and the shape, size and location of fibers and voids).

6. Conclusion

The influence of the porosity on the transverse mechanical response of UD fiber-reinforced composites was analyzed by means of computational micromechanics. To this end, an RVE of the composite microstructure with different void volume fractions was generated and the mechanical behavior was simulated using the finite element method. Two different population of voids were explicitly represented in the RVE of the microstructure: Interfiber voids and circular voids within the matrix. The fiber behavior was elastic and isotropic while the matrix was an elasto-plastic solid following the modified Drucker–Prager yield surface proposed by Lubliner [19]. Brittle matrix failure in tension and fiber/matrix interfacial debonding were accounted for.

Porosity reduced markedly the strength of composite under transverse tension and compression although it did not modify the dominant failure mechanisms. Failure under tension was controlled by interface decohesion while in compression it was dominated by the localized plastic shear band throughout the matrix. In both cases, interfiber voids acted as stress concentrators which triggered the onset of failure at lower stresses. Circular voids in the matrix affected the localization path throughout the microstructure.

The model was also used to determine numerically the failure envelope in the σ_2–τ_{23} stress space of composite containing $V_v = 0\%$, 1%, 2% and 5%. They were in good agreement with the predictions of Puck's model (based on the transverse tensile and compressive strength provided by the computational micromechanics). This supports the validity of the computational model to predict different failure mechanisms based on the microstructural features.

Acknowledgments

The authors would like to thank Prof. Bent F. Sørensen and Dr. L.P. Canal for their ideas and comments and Mr. T. Løgstrup Andersen for providing Fig. 1. This work was supported by the Danish Council for Strategic Research (Grant No.: 09-067212) under the Danish Center for Composite Structures and Materials for Wind Turbines (DCCSM) and by the Spanish Ministry of Economy and Competitiveness under Grant MAT2012-37552.

References

[1] París F, Correa E, Cañas J. Micromechanical view of failure of the matrix in fibrous composite materials. Compos Sci Technol 2003;63:1041–52.
[2] Correa E, Mantič V, París F. A micromechanical view of inter-fibre failure of composite materials under compression transverse to the fibres. Compos Sci Technol 2008;68:2010–21.
[3] Romanowicz M. A numerical approach for predicting the failure locus of fiber reinforced composites under combined transverse compression and axial tension. Comput Mater Sci 2012;51:7–12.
[4] González C, Llorca J. Mechanical behavior of unidirectional fiber-reinforced polymers under transverse compression: microscopic mechanisms and modeling. Compos Sci Technol 2007;67:2795–806.
[5] Totry E, González C, Llorca J. Failure locus of fiber-reinforced composites under transverse compression and out-of-plane shear. Compos Sci Technol 2008;68:829–39.
[6] Thomason JL. The interface region in glass fibre-reinforced epoxy resin composites: 2. Water absorption, voids and the interface. Composites 1995;26:477–85.
[7] Hernández S, Sket F, Molina-Aldareguía JM, González C, Llorca J. Effect of curing cycle on void distribution and interlaminar shear strength in polymer–matrix composites. Compos Sci Technol 2011;71:1331–41.
[8] Olivier P, Cottu JP, Ferret B. Effects of cure cycle pressure and voids on some mechanical properties of carbon/epoxy laminates. Composites 1995;26:509–15.
[9] Jeong H. Effects of voids on the mechanical strength and ultrasonic attenuation of laminated composites. J Compos Mater 1997;31:276–92.
[10] Costa ML, Rezende MC, Almeida SFM. Strength of hygrothermally conditioned polymer composites with voids. J Compos Mater 2005;39:1943–61.
[11] Zhang AY, Li DH, Zhang DX, Lu HB, Xiao HY, Jia J. Qualitative separation of the effect of voids on the static mechanical properties of hygrothermally conditioned carbon/epoxy composites. eXPRESS Poly Lett 2005;5:708–16.
[12] Chew HB, Guo TF, Cheng L. Effects of pressure-sensitivity and plastic dilatancy on void growth and interaction. Int J Solids Struct 2006;43:6380–97.
[13] Cheng L, Guo TF. Void interaction and coalescence in polymeric materials. Int J Solids Struct 2007;44:1787–808.
[14] Moraleda J, Segurado J, Llorca J. Finite deformation of porous elastomers: a computational micromechanics approach. Philos Mag 2007;87:5607–27.
[15] Little JE, Yuan X, Jones MI. Characterisation of voids in fibre reinforced composite materials. NDT & E Int 2012;46:122–7.
[16] Kinloch AJ, Young RJ. Fracture behaviour of polymers. Elsevier Applied Science Publishers; 1983.
[17] Quinson R, Perez J, Rink M, Pavan A. Yield criteria for amorphous glassy polymers. J Mater Sci 1997;32:1371–9.
[18] Puck A, Schürmann H. Failure analysis of FRP laminates by means of physically based phenomenological models. Compos Sci Technol 2002;62:1633–62.
[19] Lubliner J, Oliver J, Oller S, Oñate E. A plastic-damage model for concrete. Int J Solids Struct 1989;25:299–329.
[20] Lee J, Fenves GL. Plastic-damage for cyclic loading of concrete structures. J Eng Mech 1998;124:892–900.
[21] Canal LP, González C, Segurado J, Llorca J. Intraply fracture of fiber-reinforced composites: microscopic mechanisms and modeling. Compos Sci Technol 2012;72:1223–32.
[22] Tvergaard V, Hutchinson JW. The influence of plasticity on mixed mode interface toughness. J Mech Phys Solids 1993;41:1119–35.
[23] Abaqus. Analysis user's manual, version 6.12. Simulia; 2012.
[24] Ghiorse SR. Effect of void content on the mechanical properties of carbon/epoxy laminates. SAMPE Quart 1993;1:54–9.
[25] Daniel IM, Luo JJ, Schubel PM, Werner BT. Interfiber/interlaminar failure of composites under multi-axial states of stress photoelastic investigation of composites. J Compos Mater 2009;69:764–71.
[26] Hinton MJ, Soden PD, Kaddour AS. Failure criteria in fiber reinforced polymer composites: the world wide failure exercise. Elsevier; 2004.
[27] Hashin Z. Failure criteria for unidirectional fiber composites. J Appl Mech 1980;47:329–34.